

# Hydrophobicity of Self-Assembled Monolayers of Alkanes: Fluorination, Density, Roughness, and Force Cutoffs

## Supplemental Information

Shane Carlson<sup>1</sup>, Maximilian Becker<sup>1</sup>, Florian N. Brüning<sup>1</sup>, Kenichi Ataka<sup>1</sup>, Rubén Cruz<sup>1</sup>, Leixiao Yu<sup>2</sup>,  
Peng Tang<sup>2</sup>, Hesam Makki<sup>3</sup>, Matej Kanduč<sup>4</sup>, Rainer Haag<sup>2</sup>, Joachim Heberle<sup>1</sup>, and Roland R. Netz<sup>1</sup>

<sup>1</sup>Fachbereich Physik, Freie Universität Berlin, Arnimallee 14, 14195 Berlin, Germany

<sup>3</sup>Polymer and Color Engineering, Amirkabir University of Technology, 424 Hafez Ave, Tehran, Iran, 15875-4413

<sup>4</sup>Institut für Chemie und Biochemie, Freie Universität Berlin, 14195, Berlin, Germany

<sup>4</sup>Department of Theoretical Physics, Jožef Stefan Institute, Jamova cesta 39, 1000 Ljubljana, Slovenija

August 4, 2021

### S1 Modified Young's Equation

The modified Young's equation relates the contact angle  $\theta$  of a spherical-section-shaped liquid droplet on a flat solid surface to the droplet footprint radius  $a$ , the surface tensions  $\gamma_{sl}$ ,  $\gamma_{sv}$  and  $\gamma_{lv}$  of the solid-liquid, solid-vapor, and liquid-vapor interfaces, and the line tension  $\tau$  of the solid-liquid-gas triphasic line.

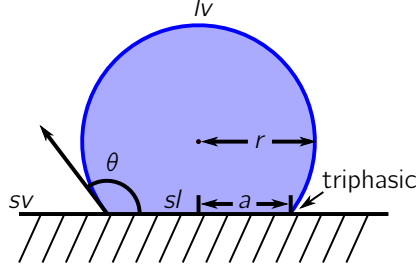


Figure S1: Schematic illustrating a droplet on a solid surface. The three biphasic interfaces and triphasic line, as well as the droplet radius  $r$ , droplet footprint radius  $a$ , and contact angle  $\theta$ , are indicated.

For a droplet adsorbed on a flat solid surface, there is a free energy cost  $F_{\mu\nu}$  to each interface that is proportional to its area  $A_{\mu\nu}$ , and to the triphasic line that is proportional to its length  $L$ , so the interfacial free energy of the adsorbed droplet is given by

$$F_{\text{ads}} = F_{sl} + F_{sv} + F_{lv} + F_{\text{triphasic}} \quad (\text{S1})$$

$$= \gamma_{sl}A_{sl} + \gamma_{sv}A_{sv} + \gamma_{lv}A_{lv} + \tau L. \quad (\text{S2})$$

The areas of the three interfaces and length of the triphasic line are given by

$$A_{sl} = \pi r^2 \sin^2 \theta, \quad A_{sv} = A_{\text{surface}} - A_{sl}, \quad A_{lv} = 2\pi r^2 (1 - \cos \theta), \quad L = 2\pi r \sin \theta, \quad (\text{S3})$$

where  $r$  is the droplet radius as illustrated in Figure S1.  $A_{\text{surface}}$  is the constant area of the planar surface, so  $\frac{dA_{sl}}{d\theta} = -\frac{dA_{sv}}{d\theta}$ . The system should relax to a free energy minimum, so

$$\frac{dF_{\text{ads}}}{d\theta} = \gamma_{sl} \frac{dA_{sl}}{d\theta} + \gamma_{sv} \frac{dA_{sv}}{d\theta} + \gamma_{lv} \frac{dA_{lv}}{d\theta} + \tau \frac{dL}{d\theta} \quad (\text{S4})$$

$$= \Delta\gamma_s \frac{dA_{sl}}{d\theta} + \gamma_{lv} \frac{dA_{lv}}{d\theta} + \tau \frac{dL}{d\theta} = 0, \quad (\text{S5})$$

where  $\Delta\gamma_s \equiv \gamma_{sl} - \gamma_{sv}$ . The volume of the droplet

$$V = \frac{\pi}{3} r^3 (2 + \cos \theta) (1 - \cos \theta)^2, \quad (\text{S6})$$

should remain constant under relaxation. Setting its total derivative with respect to  $\theta$  to zero yields

$$\frac{dr}{d\theta} = \frac{-r \sin \theta (1 + \cos \theta)}{(2 + \cos \theta) (1 - \cos \theta)}. \quad (\text{S7})$$

The total derivatives of  $A_{sl}$ ,  $A_{lv}$  and  $L$  with respect to  $\theta$  are taken, and by substituting the result for  $\frac{dr}{d\theta}$  in Equation (S7), can be written as

$$\frac{dA_{sl}}{d\theta} = -2\pi r^2 \frac{\sin \theta}{2 + \cos \theta}, \quad \frac{dA_{lv}}{d\theta} = \frac{dA_{sl}}{d\theta} \cdot \cos \theta, \quad \frac{dL}{d\theta} = \frac{dA_{sl}}{d\theta} \cdot \frac{1}{r \sin \theta}. \quad (\text{S8})$$

Substituting these expressions into Equation (S5) gives

$$\left( \Delta\gamma_s + \gamma_{lv} \cos \theta + \frac{\tau}{r \sin \theta} \right) \frac{dA_{sl}}{d\theta} = 0. \quad (\text{S9})$$

Geometry demands that  $\frac{dA_{sl}}{d\theta} \neq 0$ . This, coupled with the fact that  $a = r \sin \theta$  gives

$$\Delta\gamma_s + \gamma_{lv} \cos \theta + \frac{\tau}{a} = 0. \quad (\text{S10})$$

As the droplet size and therefore droplet footprint radius  $a$  tend to infinity, the line-tension term vanishes, giving Young's equation

$$\cos \theta_0 = \frac{\gamma_{sv} - \gamma_{sl}}{\gamma_{lv}}, \quad (\text{S11})$$

where  $\theta_0$  is the contact angle in the macroscopic limit. Equation (S11) may be resubstituted into Equation (S10) to give the modified Young's equation

$$\cos \theta = \cos \theta_0 - \frac{\tau}{\gamma_{lv} a}. \quad (\text{S12})$$

Thus, finite size effects in  $\cos \theta$  from the line tension  $\tau$  are expected to scale like  $1/a$ , and the macroscopic contact angle  $\theta_0$  can be recovered by extrapolating  $\cos \theta$  to the  $a \rightarrow \infty$  limit.

## S2 Interaction Energy in Continuum Approximation

Consider a liquid droplet adsorbed on a flat solid surface, each consisting of one type of atom only. Approximating the liquid and solid as continua, the interaction energy between the two can be written

$$E_{\text{int}} = - \int d\mathbf{r} \tilde{n}_l(\mathbf{r}) \int d\mathbf{r}' \tilde{n}_s(\mathbf{r}') \tilde{V}(|\mathbf{r}' - \mathbf{r}|), \quad (\text{S13})$$

where  $\tilde{n}_l$  and  $\tilde{n}_s$  are number densities of the liquid and solid respectively, and  $\tilde{V}(r)$  is the interaction potential between liquid and solid. The minus sign in Equation (S13) is there because we are taking  $E_{\text{int}}$  to be *positive* for an attractive surface. Assume that  $\tilde{V}(r)$  decays to zero for large  $r$ , becoming insignificant over a distance on the order of nanometers. Next, it is assumed that the number densities inside the continua are constant. Thus, there exists a function  $n_s(z) = \tilde{n}_s(\mathbf{r})$ , and

$$E_{\text{int}} = - \int d\mathbf{r} \tilde{n}_l(\mathbf{r}) \int dz' n_s(z') \int_{-\infty}^{\infty} dx' \int_{-\infty}^{\infty} dy' \tilde{V}(|\mathbf{r}' - \mathbf{r}|) \quad (\text{S14})$$

$$= - \int d\mathbf{r} \tilde{n}_l(\mathbf{r}) \int dz' n_s(z') \int_{-\infty}^{\infty} d(x' - x) \int_{-\infty}^{\infty} d(y' - y) \tilde{V}(|\mathbf{r}' - \mathbf{r}|) \quad (\text{S15})$$

$$= - \int d\mathbf{r} \tilde{n}_l(\mathbf{r}) \int dz' n_s(z') V(|z' - z|), \quad (\text{S16})$$

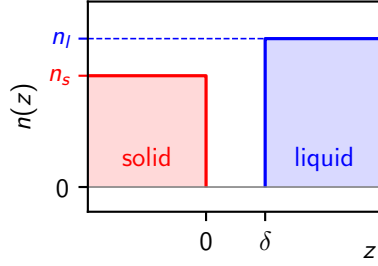


Figure S2: Schematic illustrating the continuum approximations used in the derivation of Equation (S19).

with

$$V(|z|) \equiv \int_{-\infty}^{\infty} dx \int_{-\infty}^{\infty} dy \tilde{V}(r). \quad (\text{S17})$$

In the macroscopic limit, the distance over which  $\tilde{V}(r)$  is significant is much smaller than the droplet footprint radius  $a$ , i.e. only the bottom layer of the droplet interacts with the solid. This can be approximated as a wafer-like flat cylinder of area  $A_{sl}$ , giving the areal interaction energy

$$\varepsilon_{\text{int}} = \frac{E_{\text{int}}}{A_{sl}} = - \int dz n_l(z) \int dz' n_s(z') V(|z' - z|). \quad (\text{S18})$$

Take the solid density to be  $n_s$  for  $z \leq 0$ , and zero otherwise. Further, assume there is a depletion layer of thickness  $\delta \ll R$  between the solid and liquid, such that the liquid density is  $n_l$  for  $z \geq \delta$ , and zero otherwise, as shown in Figure S2. Thus

$$\varepsilon_{\text{int}} = -n_s n_l \int_{\delta}^{\infty} dz \int_{-\infty}^0 dz' V(|z' - z|). \quad (\text{S19})$$

### S3 Scaling of Interaction Energy in Lennard-Jones Cutoff

This derivation builds upon Section S2. First, take  $\tilde{V}$  to be the Lennard-Jones potential, set to zero beyond the cutoff distance  $R$ , and only consider the long-range attractive term. In simplified units,

$$\tilde{V}(r) = -\frac{H(R-r)}{r^6}, \quad (\text{S20})$$

where  $H$  is the Heaviside step function. Thus, with reference to Equation (S17),

$$V(|z|) = - \int_{-\infty}^{\infty} dx \int_{-\infty}^{\infty} dy \frac{H(R-r)}{r^6}. \quad (\text{S21})$$

Transforming to polar coordinates  $s$  and  $\phi$  where  $x = \cos \phi$ ,  $y = \sin \phi$ ,  $s^2 = x^2 + y^2$ , and thus  $r^2 = s^2 + z^2$ , and using that  $H(R-r) = H(R^2 - r^2) = H(R - |z|)H(\sqrt{R^2 - z^2} - s)$  gives the more tractable integral

$$V(|z|) = -H(R - |z|) \int_0^{2\pi} d\phi \int_0^{\infty} ds \frac{s}{(s^2 + z^2)^3} H(\sqrt{R^2 - z^2} - s) \quad (\text{S22})$$

$$= -2\pi H(R - |z|) \int_0^{\sqrt{R^2 - z^2}} ds \frac{s}{(s^2 + z^2)^3} \quad (\text{S23})$$

$$= -\frac{\pi}{2} H(R - |z|) \left( \frac{1}{z^4} - \frac{1}{R^4} \right). \quad (\text{S24})$$

Equation (S24) may be substituted into Equation (S19) giving

$$\varepsilon_{\text{int}} = \frac{\pi}{2} n_s n_l \int_{\delta}^{\infty} dz \int_{-\infty}^0 dz' H(R - |z - z'|) \left( \frac{1}{(z - z')^4} - \frac{1}{R^4} \right) \quad (\text{S25})$$

$$= \frac{\pi}{2} n_s n_l \int_{\delta}^R dz \int_{z-R}^0 dz' \left( \frac{1}{(z - z')^4} - \frac{1}{R^4} \right). \quad (\text{S26})$$

These integrals may be solved analytically, giving

$$\varepsilon_{\text{int}} = \frac{\pi}{12} n_s n_l \left( \frac{1}{\delta^2} - \frac{6}{R^2} + \frac{8\delta}{R^3} - \frac{3\delta^2}{R^4} \right). \quad (\text{S27})$$

Thus, the  $R$ -dependent part of the areal interaction energy between the liquid and solid scales to leading order like  $R^{-2}$ . Since  $\delta \ll R$ , the  $\delta/R^3$  and  $\delta^2/R^4$  terms are insignificant and the  $R^{-2}$  term gives the predominant scaling behavior of  $\varepsilon_{\text{int}}$  in  $R$ .

## S4 Interaction Energy and Entropy in Work of Adhesion

The work of adhesion, i.e. the work to isothermally completely detach a macroscopic droplet from a flat solid surface, is given by the Young-Dupré equation

$$W = A_{sl} (\gamma_{lv} - \gamma_{sl} + \gamma_{sv}) = A_{sl} \gamma_{lv} (1 + k), \quad (\text{S28})$$

where  $k = \cos \theta_0$  is the wetting coefficient. The work of adhesion  $W$  corresponds to a free energy, and may be written as

$$W = \Delta F = \Delta U - T\Delta S \quad (\text{S29})$$

where  $U$  is the internal energy,  $S$  the entropy, and  $T$  the constant temperature. Here,  $\Delta$  indicates the difference between quantities in detached and adsorbed states,  $\Delta x \equiv x_{\text{det}} - x_{\text{ads}}$ . Introducing the areal definitions

$$w = \frac{W}{A_{sl}}, \quad \Delta u = \frac{\Delta U}{A_{sl}}, \quad \Delta s = \frac{\Delta S}{A_{sl}}, \quad (\text{S30})$$

allows Equation (S29) to be rewritten as

$$w = \Delta u - T\Delta s. \quad (\text{S31})$$

See that  $w$  must be positive-valued, because otherwise the droplet would spontaneously detach from the surface. The entropy for the detached state is expected to be larger than for the adsorbed state, because liquid at a solid-liquid interface is ordered and the motion of an adsorbed droplet is restricted. Thus  $\Delta s$  is positive, and  $-T\Delta s$  reduces  $w$ . Since  $w$  is positive, the change in energy  $\Delta u$  must be positive, and larger than  $T\Delta s$ .  $\Delta u$  and  $\Delta s$  each comprise contributions due to liquid-liquid and solid-solid interactions and contributions due to solid-liquid interactions,

$$\Delta u = \Delta u^* + \varepsilon_{\text{int}}, \quad \Delta s = \Delta s^* + \Delta s_{\text{int}}, \quad (\text{S32})$$

where the starred quantities are the summed liquid-liquid and solid-solid contributions, and those labeled “int” are the solid-liquid interaction contributions. We refer to  $\Delta s_{\text{int}}$  as the adhesion entropy. It has been shown that  $\Delta u^* = T\Delta s^*$  [1]. This leaves only the areal interaction energy and adhesion entropy, giving

$$w = \varepsilon_{\text{int}} - T\Delta s_{\text{int}}. \quad (\text{S33})$$

Rearranging Equation (S33) and substituting Equation (S28) for  $w$  gives the entropic contribution

$$T\Delta s_{\text{int}} = \varepsilon_{\text{int}} - \gamma_{lv} (1 + k). \quad (\text{S34})$$

From Ref. [2], the surface tension of SPC/E water at 300 K is found to be  $\gamma_{lv} = 63.6 \text{ mJ/m}^2$ . The areal interaction energy  $\varepsilon_{\text{int}}$  is obtained from slab simulations by summing over pairwise SAM-water

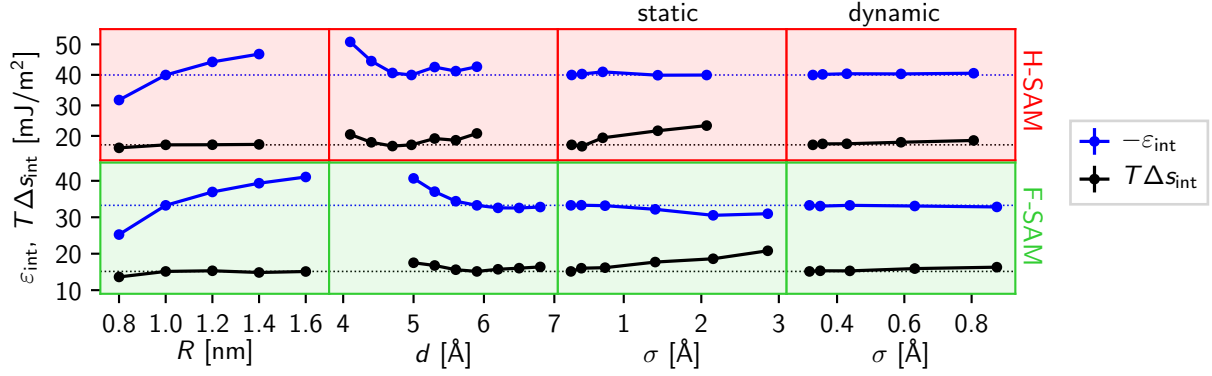


Figure S3: Areal interaction energies  $\varepsilon_{\text{int}}$  and adhesion entropy estimates  $T\Delta s_{\text{int}}$  (calculated via Equation (S33)) for H-SAMs and F-SAMs as a function of Lennard-Jones cutoff  $R$ , SAM grafting distance  $d$ , and roughness  $\sigma$ , engendered both statically and dynamically. The horizontal dotted lines show the respective values for the default SAMs, i.e. Lennard-Jones cutoff distance  $R = 1.0$  nm, restraint potential  $k = 25000$  kJ/(mol nm<sup>2</sup>), static roughness offset  $\Delta z_r = 0$ , and grafting distance  $d = 4.97$  Å for H-SAMs and  $d = 5.90$  Å for F-SAMs.

interactions. The wetting coefficient  $k = \cos \theta_0$  is obtained via droplet extrapolation technique. Thus, the entropic contribution  $T\Delta s_{\text{int}}$  may be estimated from Equation (S34) for any of the systems simulated in the main work. The results for H-SAMs and F-SAMs over Lennard-Jones cutoff distance  $R$ , SAM grafting distance  $d$ , and roughness  $\sigma$  (for both static and dynamic roughness) are shown in Figure S3. Here, it is clear that the magnitude of the energetic term is always much larger, being nearly everywhere greater than double the entropic term. Further, the entropic terms scale similarly to, but less strongly than, the interaction energy terms for varying  $d$  and  $R$  for both H-SAMs and F-SAMs. This, coupled with the fact that  $\varepsilon_{\text{int}} = 0 \Rightarrow w = 0$ , leads to the conclusion that for the parameter regimes studied,

$$w(R) \approx \kappa \varepsilon_{\text{int}}(R), \quad (\text{S35})$$

$$w(d) \approx \kappa \varepsilon_{\text{int}}(d), \quad (\text{S36})$$

where  $\kappa$  is a constant. On the other hand, increasing nanoroughness causes the entropic contribution to change more than the energetic contribution, and adhesion entropy reduction at nanoroughened surfaces should be regarded as the main cause of their elevated hydrophobicity.

## S5 Gold/Water Interaction Energy and Hamaker Constant

In the main work, SAMs are simulated with vacuum below, whereas in real systems the SAMs are fixed to a gold surface. Here, we estimate the difference the interaction of the water with the gold surface under the SAM would make in case of an infinite cutoff for H-SAMs and F-SAMs. We take smooth SAMs and the default spacing  $d_{\text{H}} = 4.97$  Å and  $d_{\text{F}} = 5.90$  Å.

We begin with Equation (S27), where the attractive Lennard-Jones potential is given by  $-B/r^6$  (instead of  $-1/r^6$ ), the Lennard-Jones cutoff distance  $R$  is set to infinity, and contributions from O and H atoms are summed,

$$\varepsilon_{\text{int}}^{\text{Au}} = \frac{\pi}{12} \frac{n_{\text{Au}}(n_{\text{O}}B_{\text{AuO}} + n_{\text{H}}B_{\text{AuH}})}{\delta^2}. \quad (\text{S37})$$

The relevant values for the London coefficients for Au-O and Au-H interactions are found in Ref. [3] to be  $B_{\text{AuO}} = 7.4675861 \cdot 10^{-3}$  kJ/mol nm<sup>6</sup> and  $B_{\text{AuH}} = 1.2886163 \cdot 10^{-3}$  kJ/mol nm<sup>6</sup>. Number densities for solid gold and liquid water are calculated from their respective mass densities under standard conditions,  $\rho_{\text{Au}} = 19.30$  g/cm<sup>3</sup> and  $\rho_{\text{H}_2\text{O}} = 0.9982$  g/cm<sup>3</sup>. The spacing between the water slab and gold surface  $\delta$  is taken to be the sum of the distances between the gold surface and the restraint positions of the

bottom C atoms of the SAM,  $\delta_{\text{Au}-r}$  and between the restraint positions and Gibbs dividing surface of the water,  $\delta_{r-\text{GDS}}$ . The distance  $\delta_{r-\text{GDS}}$  is obtained directly from slab simulations, and is found to be 1.28 nm for the H-SAM and 1.35 nm for the F-SAM. The distance  $\delta_{\text{Au}-r}$  is estimated from Ref. [4] to be between 2.98 and 3.73 Å, and depends on whether S atoms are taken to bind on top of Au atoms or above hollow sites in the Au(111) surface. Substituting these values into Equation (S37) gives  $\varepsilon_{\text{int}}^{\text{Au}} = 3.30 \pm 0.15$  mJ/m<sup>2</sup> for the H-SAM and  $3.03 \pm 0.14$  mJ/m<sup>2</sup> for the F-SAM. By comparison, the areal dispersive SAM-water interaction energies in the  $R \rightarrow \infty$  limit for the H-SAM and F-SAM are found to be  $\varepsilon_{\text{int}}^{\text{LJ}} = 54.23 \pm 0.01$  mJ/m<sup>2</sup> and  $46.31 \pm 0.03$  mJ/m<sup>2</sup> respectively (see Figure 3c in the main work). Thus  $\varepsilon_{\text{int}}^{\text{Au}}$  is roughly 6.0% and 6.5% as large as  $\varepsilon_{\text{int}}^{\text{LJ}}$  for the H-SAM and F-SAM respectively.

The areal work of adhesion  $w$  should be expected to increase upon inclusion of the gold surface; call this larger Au-adjusted areal work of adhesion  $w^*$ . Equation (S35) implies that upon inclusion of the gold surface, the work of adhesion should scale in the same manner as does the interaction energy,

$$\frac{w^*}{w} = \frac{\varepsilon_{\text{int}}^{\text{LJ}} + \varepsilon_{\text{int}}^{\text{Au}}}{\varepsilon_{\text{int}}^{\text{LJ}}} \Rightarrow w^* = (1 + \zeta)w, \quad (\text{S38})$$

where  $\zeta \equiv \varepsilon_{\text{int}}^{\text{Au}}/\varepsilon_{\text{int}}^{\text{LJ}}$ . From (S38), a corrected wetting coefficient  $k^*$  and contact angle  $\theta^*$  may be calculated. Starting from Equation (S11), namely using that  $w = \gamma_{lv}(1 + k)$ , it follows that

$$k^* = k + \zeta(1 + k), \quad \theta^* = \arccos[k + \zeta(1 + k)]. \quad (\text{S39})$$

For the H-SAM, the contact angle in the  $R \rightarrow \infty$  limit is  $\theta = 115.4^\circ$ , from which Equation (S39) gives an adjusted angle of  $\theta^* = 113.2^\circ$ , and for the F-SAM,  $\theta = 121.4^\circ$  and  $\theta^* = 119.3^\circ$ . Thus in both cases, we estimate inclusion of the gold surface to reduce the water contact angle only by about  $2^\circ$ . These corrections are shown in Figure 3d in the main work.

The number densities and London coefficients may also be used to obtain the Hamaker constant, which parametrizes the interaction strength between two materials [5]. The Hamaker constant may be written

$$A = \pi^2 \sum_{i,j} n_i n_j B_{ij}, \quad (\text{S40})$$

where  $i$  and  $j$  each index atom types in one of the two respective materials. We wish to compare the Hamaker constants of solid gold-water and SAM-water for both H-SAMs and F-SAMs. The average SAM number densities are found from SAM-water slab simulations to be (in nm<sup>-3</sup>) for the H-SAM:  $n_C = 39.4$  and  $n_H = 79.2$ , and for the F-SAM:  $n_C = 27.0$  and  $n_F = 53.8$ . The London coefficients for the SAMs are calculated directly from the relevant OPLS-AA Lennard-Jones parameters as  $B_{ij} = 4\varepsilon_{ij}\sigma_{ij}^6$ . The resulting H-SAM-water and F-SAM-water Hamaker constants are  $7.33 \cdot 10^{-20}$  and  $6.99 \cdot 10^{-20}$  J respectively. The gold-water Hamaker constant is found from the number densities and London coefficients above to be  $3.24 \cdot 10^{-19}$  J. Thus, H-SAMs and F-SAMs are 22.6% and 21.6% as attractive to water as an equal volume of solid gold at an equal distance, respectively.

## S6 Contact Angle Goniometry

H-SAMs and F-SAMs are prepared using dip-coating of 1-decanethiol and 1H,1H,2H,2H-perfluorodecanthiol on gold slides (Au(111) on mica, PHASIS), respectively. The freshly cleaned gold slides are incubated in the solution of 1H,1H,2H,2H-perfluorodecanethiol or 1-decanethiol solution (1 mM in ethanol) at room temperature for 24 hours. Afterwards, the coated slides are removed, thoroughly rinsed with ethanol, dried with nitrogen blowing, and again dried in vacuum for another 24 hours. The static contact angle measurements are performed with a contact angle goniometer (DataPhysics Instruments, Germany) using the sessile drop method. A liquid drop of 2  $\mu\text{L}$  Milli-Q water is placed on the substrate and allowed to equilibrate for 15 s at room temperature. At least fifteen measurements from five different samples are averaged in order to obtain a standard deviation and assess measurement reproducibility.

The advancing and receding contact angles on the SAMs are quantified using a method similar to that reported by Korhonen et al. [6]. To measure the advancing contact angle, a sessile drop of 2  $\mu\text{L}$  of water is first dispensed on the surface with the dispensing unit (needle) remaining in the water droplet. Water is then slowly dispensed into the droplet at a rate of 0.1  $\mu\text{L}/\text{s}$ . Even as the volume of the droplet increases, the contact line at the base of the droplet tends to remain stable temporarily, causing the contact angle to increase. During this process, the contact angle is automatically measured and recorded twice per second. Once the volume becomes “saturated”, the contact line begins to advance, and the corresponding contact angle is taken as the advancing contact angle  $\theta_a$ . Measurement of the receding contact angle is similar to that for the advancing contact angle, except in reverse: water is continuously removed from the droplet until the droplet contact line begins to recede, with the corresponding contact angle taken as the receding contact angle. The resulting contact angle measurements are reported in Table S1.

	$\theta_r$	$\theta_s$	$\theta_a$
H-SAM	$89.9 \pm 2.7^\circ$	$98.4 \pm 2.4^\circ$	$107.6 \pm 3.1^\circ$
F-SAM	$99.7 \pm 2.6^\circ$	$102.3 \pm 2.2^\circ$	$113.2 \pm 2.5^\circ$

Table S1: Experimental receding, static and advancing contact angles of H-SAMs (1-decanethiol) and F-SAMs (1H,1H,2H,2H-perfluordecantiol) on Au(111).

## S7 F-SAM Tilt Angle via SEIRAS

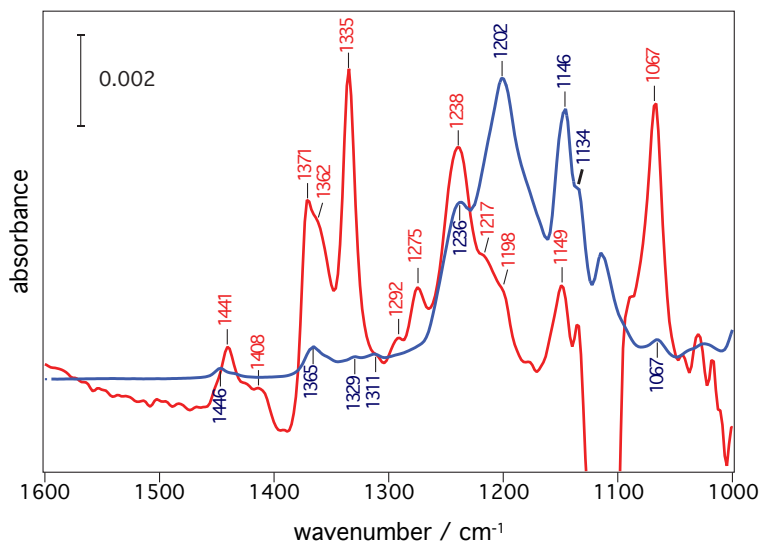


Figure S4: SEIRA spectrum of the self-assembled monolayer of heptadecafluorodecane thiol (H2F8) bound to the rough gold surface (red curve). The blue curve represents the normalized spectrum of the bulk sample recorded by the attenuated total reflection method.

The tilt angle of an F-SAM on Au was determined from surface enhanced infrared absorption spectroscopy (SEIRAS). Figure S4 shows the SEIRA spectrum (solid red) of the F-SAM, comprising  $\text{SH}(\text{CH}_2)_2(\text{CF}_2)_7\text{CF}_3$  or H2F8 molecules, covalently adsorbed via the terminal thiol on a gold film surface. The FTIR spectrum of bulk H2F8 (blue curve) which represents an isotropic distribution of H2F8 molecules, was recorded in attenuated total reflection (ATR) geometry. The SEIRA spectrum represents the orientated F-SAM and is similar to the IRRAS spectrum reported by Chidsey et al. [7]. When comparing the spectra of the F-SAM and the isotropic bulk sample, striking differences are observed in the intensities of the bands. Strong bands between  $\sim 1200$  and  $1146 \text{ cm}^{-1}$  in the ATR spectrum of the isotropic sample significantly

decrease in relative intensities in the SEIRA spectrum of the F-SAM. Most of the bands in this region were assigned to normal modes with a transition dipole moment perpendicular to the molecular axis (perpendicular component). In contrast, the relative intensities of the bands at 1371, 1362, 1335, and 1238  $\text{cm}^{-1}$  are drastically increased in the SEIRA spectrum. These bands correspond to vibrational modes with an associated transition dipole moment oriented along the helical backbone axis (axial component). The increase and decrease in the relative intensities of the two groups of bands can be explained in terms of the molecular orientation of the F-SAM and the surface selection rule of SEIRAS. In SEIRAS, only the transition dipole moment component parallel to the surface normal is selectively enhanced. This effectively leads to spectral shapes similar to the ones obtained from p-polarized measurements conducted by IRRAS. The molecular tilt angle is retrieved from the comparison of the relative intensities of the axial and perpendicular bands in the isotropic and F-SAM spectra (see below for details). Our analysis resulted in a tilt angle for the F-SAM of  $16 \pm 4^\circ$  which agrees with reported IRRAS data on F-SAMs bound to the Au(111) surface.

### S7.1 Calculation of Vibrational Normal Modes and Dipole Derivatives

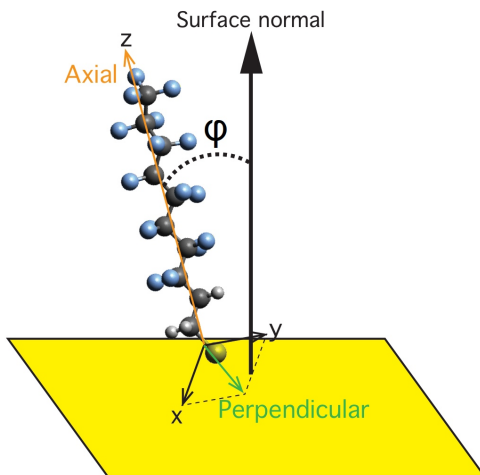


Figure S5: The molecular and surface coordinates of an idealized H2F8 molecule on a gold surface. The helical axis of the H2F8 molecule is defined as z-axis of the molecular reference frame. Bands with a transition dipole moment (TDM) parallel to this direction are referred as “axial” or “out-of-plane” bands. Accordingly, bands with a TDM contained within the XY plane are referred as “perpendicular bands” or “in-plane” bands. Tilt angle  $\phi$  is defined as the angle formed between the axial component and the surface normal.

The vibrational normal modes of a single H2F8 molecule in vacuum were calculated by the *Gaussian09* program package using B3LYP,6-31G(d,p) level of theory. This calculation also provides the Cartesian coordinates of the transition dipole moment (TDM) of all normal modes, which can be used to calculate the absorptivity of each band for different polarizations of the IR electric field (EF). The molecular reference frame shown in Figure S5 was adopted to describe our system. The helical axis was chosen as the z-axis of the molecular reference frame. Because H2F8 adopts a helical structure, any rotation around the helical axis produces an invariable IR spectrum for a fixed EF polarization. To account for this effect, the contribution to the intensity of each normal mode is decomposed into “axial” (out-of-plane) and “perpendicular” (in-plane) components. These components are calculated from the TDM coordinates as  $\text{TDM}z^2$  (axial) and  $\text{TDM}x^2 + \text{TDM}y^2$  (in-plane). These definitions result from averaging the expected absorptivity of a given mode for all possible twist angles, a detailed description of which can be found in Ref. [8]. It should be noted that only half of the in-plane intensity as defined is observed in the polarized spectrum of a single molecule ( $(\text{TDM}x^2 + \text{TDM}y^2)/2$ ). The most relevant normal modes in the region between 1000 and 1500  $\text{cm}^{-1}$  are compiled in Table S2 along with their molar absorptivity for each direction.

Experimental		DFT calculation					Assignment			
Wavenumber (SEIRAS) / $\text{cm}^{-1}$	Wavenumber (ATR) / $\text{cm}^{-1}$	Wavenumber (DFT) / $\text{cm}^{-1}$	Integrated molar absorptivity (km/mol)	Axial molar absorptivity (km/mol)	In-plane molar absorptivity (km/mol)	Absorptivity percentage along axis (%)	Symmetry species	Description		
R. I.	R. I.									
1360	0.83	1366	0.11	1408	12.87	10.56	2.31	82.051	$A_2$	C(9)H <sub>2</sub> wag, C(10)H <sub>2</sub> twist (localized to CH <sub>2</sub> moieties)
1372	0.91	1352	0.07	1385	33.93	32.46	1.46	95.696	$A_2$	C(1)F <sub>3</sub> in-phase def. C(2)F <sub>2</sub> sym. str. coupled with C(1)-C(2) str.
1334	1.41	1330	0.08	1345	63.32	63.24	0.09	99.858	$A_2$	C(1)F <sub>3</sub> in-phase def. C(2)F <sub>2</sub> sym. str. coupled with C(1)-C(2)-C(3) asym. str., C(9)H <sub>2</sub> , C(10)H <sub>2</sub> twist
1310	0.29	1312	0.08	1323	11.27	0.99	10.28	8.784	$E_1$	C(2-7)F <sub>2</sub> wag, C(8)F <sub>2</sub> sym. str. coupled with C-C-C asym. str., C(9)H <sub>2</sub> twist
1294	0.34	1294	0.08	1306	21.00	0.34	20.66	1.619	$E_1$	C(2,5,8)F <sub>s</sub> sym. str., C(3,4,6,7)F <sub>s</sub> wag. coupled with C(2-4), C(6,7,8) asym. str.
1276	0.52	1282	0.09	1285	22.89	18.49	4.40	80.778	$A_2$	C(1)F <sub>3</sub> out-of-phase str. C(4,7)F <sub>2</sub> wag, C(3,5)F <sub>2</sub> sym. str. coupled with C(3)-C(4)-C(5), C(6)-C(7)-C(8) asym. str.
1240	1.00	1242	0.59	1271	535.22	6.22	529.00	1.162	$E_1$	C(1)F <sub>3</sub> out-of-phase str. C(2-7)F <sub>2</sub> asym. str. coupled with C-C-C bending
1214	0.56	1214		1258	167.85	2.81	165.04	1.674	$E_1$	C(1)F <sub>3</sub> out-of-phase str., C(4,5,6)F <sub>2</sub> def.
1200	0.36	1200	1.00	1246	164.87	7.58	157.29	4.598	$E_1$	C(1)F <sub>3</sub> out-of-phase str. C(2-8)F <sub>2</sub> asym. str. coupled with C-C-C bending, C(9)H <sub>2</sub> def. and C(10)H <sub>2</sub> twist
1148	0.36	1146	0.90	1237	266.03	0.01	266.02	0.004	$E_1$	C(1)F <sub>3</sub> out-of-phase str. C(2-8)F <sub>2</sub> asym. str. coupled with C-C-C bending and C(10)H <sub>2</sub> twist
1134	0.18	1132	0.64	1219	169.43	1.06	168.70	0.624	$E_1$	C(2-4)F <sub>2</sub> sym. str., C(5-8)F <sub>2</sub> asym. str. C(1)-C(2)-C(3), C(4)-C(5)-C(6), C(7)-C(8)-C(9) bending
		1114	0.42	1174	246.73	13.56	233.17	5.496	$E_1$	C(2-7)F <sub>2</sub> sym. str., C(8)F <sub>2</sub> def
1068	1.04	1064	0.13	1135	46.55	1.08	45.46	2.321	$E_1$	C(1)F <sub>3</sub> in-phase def., C(2-8)F <sub>2</sub> sym. str. C(1)-C(2)-C(3), C(4)-C(5)-C(6), C(7)-C(8) bending

Table S2: Experimental and calculated IR absorption bands of heptadecafluorodecane thiol (H2F8). R.I. indicates relative peak intensities with respect to the peaks found at  $1240 \text{ cm}^{-1}$  (SEIRAS) and  $1200 \text{ cm}^{-1}$  (ATR).

## S7.2 Band Deconvolution of the Experimental Spectra

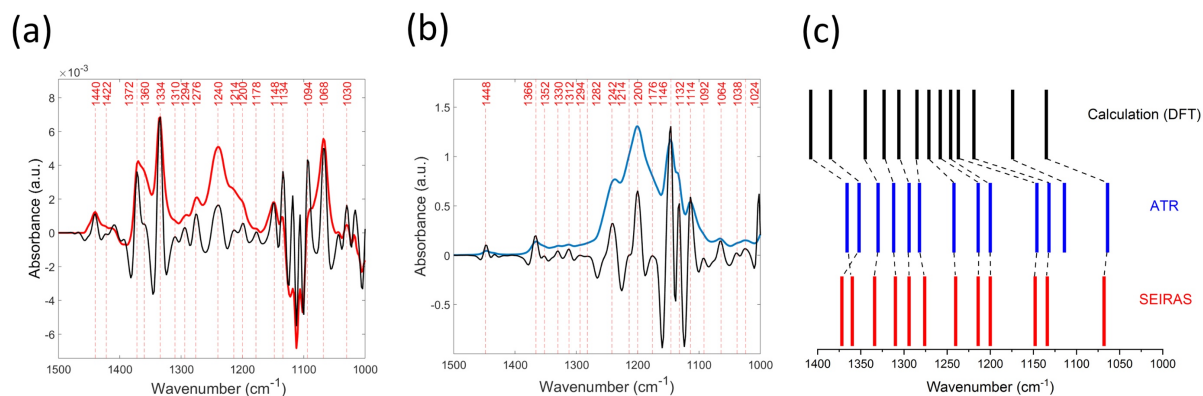


Figure S6: IR absorption and wavelet deconvolution (resized) of H2F8 in (a) Self-assembled monolayer and (b) Bulk sample. (c) Correlation diagram between the bands from the calculation (black), bulk sample (blue) and F-SAM (red).

The band broadening typically observed in perfluoro-oligomers obscures the exact positions of the individual bands. To make a direct comparison with the calculated normal modes, wavelet deconvolution was applied. The continuous wavelet transform of the experimental data was calculated using a Gaussian generating function with a sigma value of  $3 \text{ cm}^{-1}$  (ATR) and  $3.58 \text{ cm}^{-1}$  (SEIRAS). A threshold of 3% for the intensity of the local maxima was used to avoid introducing peaks from noise. The results of the wavelet deconvolution are shown in Figure S6a and b, for the bulk isotropic sample (blue) and SAM (red), respectively. The correlation between the peak positions in SEIRAS, ATR and DFT are shown in Figure S6c.

### S7.3 Band Assignment and Differences Between Bulk and Monolayer Spectra

Figure S4 shows a direct comparison of the SEIRA spectrum of a H2F8 SAM (red) and the ATR spectrum of an isotropic bulk sample (blue). In the latter spectrum, two prominent bands are observed at around 1200 and 1146  $\text{cm}^{-1}$ . The band features are broad and consist of clusters of several bands indicated from the shoulder peaks at 1242, 1132 and 1114  $\text{cm}^{-1}$ . These features are typically observed in the IR spectra of poly(tetrafluoroethylene) (PTFE) and assigned to various modes of  $\text{CF}_2$  vibrations in the long C–C chain [9, 10, 11, 12]. Along with these strong bands, there are minor bands observed at 1366, 1330 and 1312  $\text{cm}^{-1}$ . These bands are not observed in the IR spectrum of PTFE, but they start to appear in the short oligomers such as F14 or F20 [12]. From this observation these bands can be assigned to  $\text{CF}_2$  vibrations towards the end of  $-(\text{CF}_2)-$  chains. Overall, the features of the monolayer SEIRA spectrum correspond well to those previously reported in Refs. [7, 13, 14], except for the small bands at 1441, 1414 and 1068  $\text{cm}^{-1}$  in SEIRAS. We assigned these bands to residual DMSO used as solvent for the deposition process. This assignment was also suggested by a control experiment where the formation of the SAM layer took place in different solvents (data not shown). The gap at around 1100  $\text{cm}^{-1}$  is due to the absorption from the silicon prism used as a substrate.

When comparing the spectrum of the monolayer and the bulk samples, the most prominent difference observed is the drastic increase in relative intensity of the bands at 1372, 1360 and 1334  $\text{cm}^{-1}$ . Bands in this wavenumber region are caused by the vibrational coupling of the perfluorinated moiety with the alkyl spacer. More specifically, these bands are associated with the  $\text{CH}_2$  wagging mode coupled with the symmetric  $\text{CF}_2$  stretching and deformation vibrations. Because fluorine is heavier than carbon,  $\text{CF}_2$  stretching vibrations involve large displacements of the carbon atoms with respect to the mass center but only minimum displacements of the fluorine atoms. This is one of the major differences between  $\text{CF}_2$  and  $\text{CH}_2$  vibrational modes, where the opposite situation applies for hydrogens. The resulting deformation of the C–C backbone generates the strong coupling of the  $\text{CH}_2$  wagging and  $\text{CF}_2$  symmetric stretching modes and results in a vibrational mode with the associated TDM oriented predominantly along the molecular axis. The relative components of these modes along the  $z$ -axis and in the  $xy$ -plane are shown together with the band assignment in Table S2.

In the spectral region below 1300  $\text{cm}^{-1}$ , a strong set of bands is observed at 1242, 1200, and 1146  $\text{cm}^{-1}$  in the bulk spectrum. These are the characteristic fingerprint bands of perfluorinated molecules and are due to  $\text{CF}_2$  asymmetric stretching and deformation vibrations. The relative intensities of these bands are significantly decreased in the spectrum of the monolayer except for the band at 1240  $\text{cm}^{-1}$ . These bands with reduced relative intensities are associated with TDMs perpendicular to the helical backbone axis (perpendicular component). The relative intensity of the band at 1240  $\text{cm}^{-1}$  increases in SEIRAS, which suggests an axial TDM ( $A_2$  symmetry group). On the basis of its frequency and its relative intensity, it was however assigned to the mode at 1271  $\text{cm}^{-1}$  (DFT) with a mostly perpendicular TDM component. We do not have a satisfactory explanation for the behavior of this band, but it may be due to other phenomena, e.g. Fermi resonance with an axial component.

### S7.4 Determination of the Tilt Angle

The plasmonic enhancement exploited in SEIRAS creates a local EF oriented along the normal to the gold surface. This property, often referred as the selection rule of SEIRA spectroscopy, implies that only the TDM component normal to the gold surface of a given mode is selectively enhanced. The same property can be exploited to resolve molecular orientation. In the specific case of a helical molecule, this can be done by identifying two bands with associated TDMs perpendicular to one another, one oriented along the molecular axis and the other perpendicular to it. The tilt angle can be retrieved via the “ratio method” [15]. Intensities observed in SEIRAS are normalized with respect to those observed in an isotropic spectrum and the tilt angle  $\phi$  is calculated from the ratio of the two normalized intensities,

$$\tan^2 \phi = 2 \cdot \frac{I_p^{\text{SAM}}}{I_p^{\text{ATR}}} \cdot \frac{I_z^{\text{ATR}}}{I_z^{\text{SAM}}} \quad (\text{S41})$$

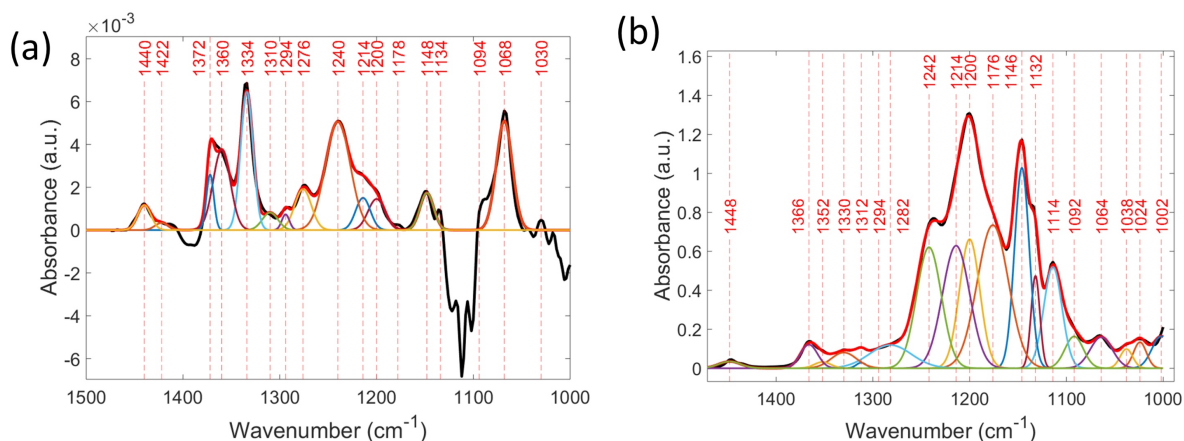


Figure S7: Fitting of experimental data with a set of Gaussian functions (Equation (S42)) centered at the wavenumber values obtained from the wavelet deconvolution method. **(a)** Self-assembled monolayer (SEIRAS). **(b)** Liquid bulk sample (ATR).

In our case, the isotropic spectrum was recorded with the attenuated total reflection technique from a liquid (bulk) sample of H2F8. To derive peak intensities, experimental data was fit with the *Matlab fitnlm* method using a set of Gaussians,

$$\sum_i \frac{I_i}{\sigma_i \sqrt{2\pi}} e^{-\frac{1}{2}(\omega - \omega_i)^2 / \sigma_i^2}, \quad (\text{S42})$$

where standard deviation  $\sigma_i$  and intensity  $I_i$  are the fitting parameters and wavenumbers  $\omega_i$  are obtained beforehand by the wavelet deconvolution method and held constant for the fit. The results from the fitting process are shown in Figure S7a and b.

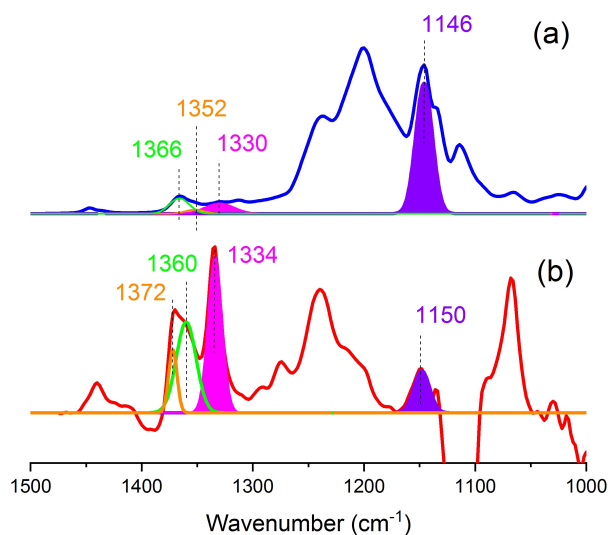


Figure S8: **(a)** ATR spectrum of H2F8 bulk sample. **(b)** SEIRA spectrum of the monolayer together with some of the peaks discussed for the estimation of the tilt angle  $\phi$ . Transition dipole moments (TDMs) associated with peaks at 1352/1372, 1366/1360 and 1330/1334  $\text{cm}^{-1}$  are oriented predominantly along the molecular axis while the TDM of the band at 1146/1150  $\text{cm}^{-1}$  is oriented perpendicular to it. The final value of  $16 \pm 4^\circ$  was obtained by comparing areas of peaks at 1330/1334 and 1146/1150  $\text{cm}^{-1}$ .

From the band assignment and the DFT calculation (Table S2), the most suitable bands to obtain the tilt angle were determined to be the modes at 1345 and 1237  $\text{cm}^{-1}$  (DFT), assigned to the experimental peaks

at 1334 and 1148  $\text{cm}^{-1}$  (SEIRAS) and 1330 and 1146  $\text{cm}^{-1}$  (ATR). These peaks have the highest and lowest axial projection, respectively, of all peaks of the list (see the along-axis absorptivity percentage in Table S2) and also benefit from being relatively isolated in the spectrum. This choice is further supported by previous pMAIRS studies [16]. The confidence interval of the tilt angle was estimated using error propagation on Equation (S41) and the standard errors from the fitting procedure.

The calculated tilt angle  $\phi = 16 \pm 4^\circ$  corresponds well to the values previously reported by Chidsey et al. determined from IRRAS [7]. In the same article they also provide other possible tilt angles of  $\phi = 15\text{-}16^\circ$  and  $\phi = 5^\circ$ , depending on the IR bands used. For comparison, we also determine the tilt angle using the other two axial bands at 1408 and 1385  $\text{cm}^{-1}$  (DFT) of the same symmetry group, which yield tilt angles of  $17 \pm 7^\circ$  and  $18 \pm 3^\circ$  respectively. However, calculation from these peaks is more prone to error due to the overlap between the two, which can lead to an uneven distribution of intensities when comparing the ATR and SEIRAS spectra. To avoid this issue, the intensities of the two peaks can also be summed and treated as a single peak in both spectra. Using this procedure, a value of  $17 \pm 4^\circ$  was obtained, quite close to the one derived from the analysis of the peak at 1345  $\text{cm}^{-1}$  (DFT).

## S8 Contact Angle as a Function of Surface Number Density

This derivation builds upon Section S2. For the case of multiple species  $\eta$  of atoms in the solid (e.g.  $\eta = \text{C, H, F}$  etc.), the areal interaction energy is just the sum over all species of the interaction energies as calculated via Equation (S19),

$$\varepsilon_{\text{int}} = \sum_{\eta} \varepsilon_{\text{int}}^{\eta} = -n_l \int_{\delta}^{\infty} dz \int_{-\infty}^0 dz' \sum_{\eta} n_s^{\eta} V^{\eta}(|z' - z|). \quad (\text{S43})$$

In the main work, the density of SAMs is varied by changing intermolecular spacing, with molecular composition unchanged. Thus the proportions of hydrogen or fluorine atoms to carbon atoms remains constant. Taking as an example an F-SAM, this implies  $n_s^{\text{F}} = \lambda n_s^{\text{C}}$  (with  $\lambda \approx 2$ ). Under this assumption, Equation (S43) gives

$$\varepsilon_{\text{int}} = -n_l \int_{\delta}^{\infty} dz \int_{-\infty}^0 dz' (n_s^{\text{C}} V^{\text{C}}(|z' - z|) + n_s^{\text{F}} V^{\text{F}}(|z' - z|)) \quad (\text{S44})$$

$$= -n_l n_s^{\text{C}} \int_{\delta}^{\infty} dz \int_{-\infty}^0 dz' (V^{\text{C}}(|z' - z|) + \lambda V^{\text{F}}(|z' - z|)) \quad (\text{S45})$$

$$= \tilde{\alpha} n_s^{\text{C}}, \quad (\text{S46})$$

where  $\tilde{\alpha}$  is a constant in  $n_s^{\text{C}}$ . In Section S4, it is shown that for varying  $d$ ,

$$w = \gamma_{lv}(1 + \cos \theta_0) \approx \kappa \varepsilon_{\text{int}}, \quad (\text{S47})$$

where  $\kappa$  is a constant. Combining Equations (S46) and (S47) and defining a new constant  $\alpha = \tilde{\alpha}\kappa/\gamma_{lv}$  gives

$$1 + \cos \theta_0 \approx \alpha n_s^{\text{C}}. \quad (\text{S48})$$

The same line of reasoning applies to H-SAMs, but the proportionality constant  $\alpha$  will in general be different.

## References

- [1] Ben-Naim, A. A simple model for demonstrating the relation between solubility, hydrophobic interaction, and structural changes in the solvent. *J. Phys. Chem.* **1978**, *82*, 874–885.

- [2] Vega, C.; de Miguel, E. Surface tension of the most popular models of water by using the test-area simulation method. *J. Chem. Phys.* **2007**, *126*, 154707.
- [3] Piana, S.; Bilic, A. The Nature of the Adsorption of Nucleobases on the Gold [111] Surface. *J. Phys. Chem. B* **2006**, *110*, 23467–23471.
- [4] Sellers, H.; Ulman, A.; Shnidman, Y.; Eilers, J. E. Structure and binding of alkanethiolates on gold and silver surfaces: implications for self-assembled monolayers. *J. Amer. Chem. Soc.* **1993**, *115*, 9389–9401.
- [5] Hamaker, H. The London–van der Waals attraction between spherical particles. *Physica* **1937**, *4*, 1058–1072.
- [6] Korhonen, J. T.; Huhtamäki, T.; Ikkala, O.; Ras, R. H. A. Reliable Measurement of the Receding Contact Angle. *Langmuir* **2013**, *29*, 3858–3863.
- [7] Chidsey, C. E. D.; Loiacono, D. N. Chemical functionality in self-assembled monolayers: structural and electrochemical properties. *Langmuir* **1990**, *6*, 682–691.
- [8] Andrews, S. S. Using Rotational Averaging To Calculate the Bulk Response of Isotropic and Anisotropic Samples from Molecular Parameters. *J. Chem. Ed.* **2004**, *81*, 877.
- [9] Masetti, G.; Cabassi, F.; Morelli, G.; Zerbi, G. Conformational Order and Disorder in Poly(tetrafluoroethylene) from the Infrared Spectrum. *Macromolec.* **1973**, *6*, 700–707.
- [10] Cho, H. G.; Strauss, H. L.; Snyder, R. G. Infrared spectra and structure of perfluoro-n-alkanes isolated in n-alkane matrixes prepared by vapor deposition. *J. Phys. Chem.* **1992**, *96*, 5290–5295.
- [11] Liang, C. Y.; Krimm, S. Infrared Spectra of High Polymers. III. Polytetrafluoroethylene and Polychlorotrifluoroethylene. *J. Chem. Phys.* **1956**, *25*, 563–571.
- [12] Naselli, C.; Swalen, J. D.; Rabolt, J. F. Order–disorder transitions in Langmuir–Blodgett films. IV. Structure of  $[\text{F}(\text{CF}_2)_8(\text{CH}_2)_{10}\text{COO}^-]_2 \text{Cd}^{2+}$  multilayers at ambient and elevated temperatures. *J. Chem. Phys.* **1989**, *90*, 3855–3860.
- [13] Lenk, T. J.; Hallmark, V. M.; Hoffmann, C. L.; Rabolt, J. F.; Castner, D. G.; Erdelen, C.; Ringsdorf, H. Structural Investigation of Molecular Organization in Self-Assembled Monolayers of a Semi-fluorinated Amidethiol. *Langmuir* **1994**, *10*, 4610–4617.
- [14] Fukushima, H.; Seki, S.; Nishikawa, T.; Takiguchi, H.; Tamada, K.; Abe, K.; Colorado, R.; Graupe, M.; Shmakova, O. E.; Lee, T. R. Microstructure, Wettability, and Thermal Stability of Semifluorinated Self-Assembled Monolayers (SAMs) on Gold. *J. Phys. Chem. B* **2000**, *104*, 7417–7423.
- [15] Debe, M. K. Extracting physical structure information from thin organic films with reflection absorption infrared spectroscopy. *J. App. Phys.* **1984**, *55*, 3354–3366.
- [16] Hasegawa, T.; Shimoaka, T.; Tanaka, Y.; Shioya, N.; Morita, K.; Sonoyama, M.; Amii, H.; Takagi, T.; Kanamori, T. An Origin of Complicated Infrared Spectra of Perfluoroalkyl Compounds Involving a Normal Alkyl Group. *Chem. Lett.* **2015**, *44*, 834–836.